Supplemental Material:

Optical Mode Control by Geometric Phase in Quasicrystal Metasurface

Igor Yulevich, Elhanan Maguid, Nir Shitrit, Dekel Veksler, Vladimir Kleiner, and Erez Hasman*

Micro and Nanooptics Laboratory, Faculty of Mechanical Engineering, and Russell Berrie Nanotechnology Institute, Technion – Israel Institute of Technology, Haifa 32000, Israel

*e-mail: mehasman@technion.ac.il

1. Tiling rule of antenna configurations

Below, we provide detailed illustrations of the anisotropic antenna tiling rule. Isotropic antennas were embedded at the middle of each edge of the Penrose tiling [Fig. S1(a)] to compose an isotropic quasicrystal metasurface (QCM.) Then, an anisotropic QCM was introduced by replacing the isotropic antennas with their anisotropic counterparts, which are oriented along the tiling grid [Fig. S1(b)].

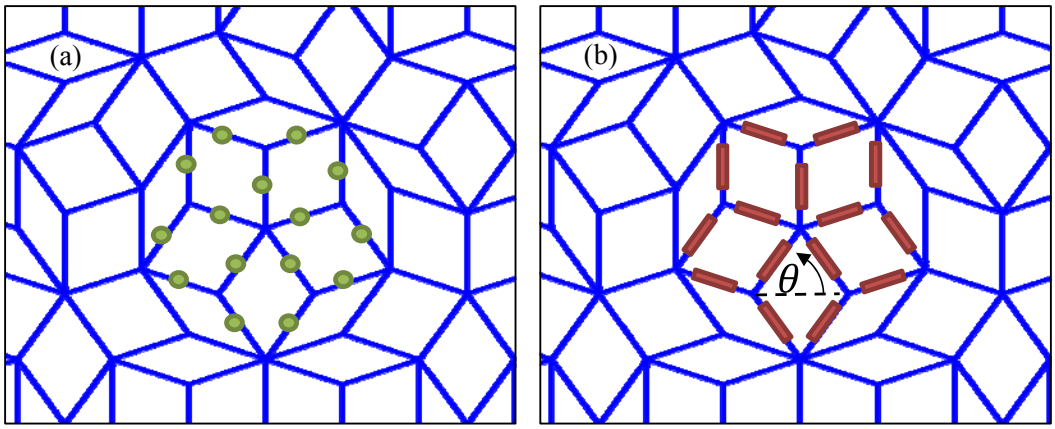

FIG. S1. Tiling rule of isotropic (a) and anisotropic (b) antenna configurations in QCM. Blue grid depicts the Penrose tiling. θ stands for the antenna orientation.

2. Local modes of the QCMs

In order to characterize the thermal emission from the metasurfaces, we distinguish between the collective and local mode excitations. The latter are modes arising as a result of the scattering from an individual subwavelength particle (nanoantenna) and are discussed below, while the former are modes obtained from the coherent collective scattering from nanoantennas of the QCM and governed by the momentum-matching condition discussed in the manuscript. Furthermore, these collective modes are the signature of surface phonon polaritons propagating along the SiC metasurface, thus providing such a coherent coupling of the localized modes into radiative modes.

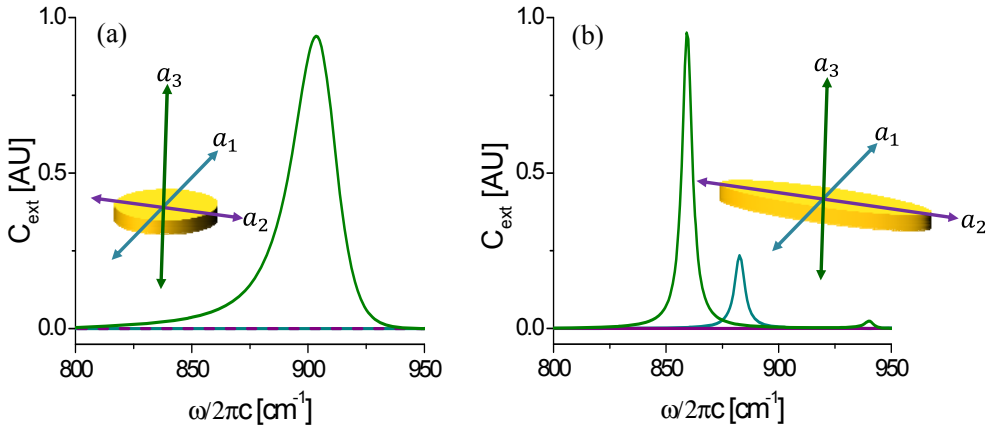

FIG. S2. (a,b) Calculated extinction cross sections of an oblate spheroid and ellipsoidal particles, respectively. The particles attained for the polarization along the semi axes a_1 (blue), a_2 (purple) and a_3 (green) exhibit corresponding resonances (blue, purple and green curves). The alternating blue-purple line in (a) denotes responses along both a_1 and a_2 axes.

Further, we provide an analysis of the local modes for isotropic and anisotropic antennas observed at $\omega_1/2\pi c = 885$ cm^{-1} in Fig. 1(c) and at $\omega_{1,2}/2\pi c = 850$ and 887 cm^{-1} in Fig. 1(d) of the manuscript. By use of the modified long wavelength approximation (MLWA) [see Ref. S1], we determine the extinction cross section $C_{ext} = k^4|\alpha_{0i}|^2/6\pi + k\,\mathrm{Im}(\alpha_{0i})$ of spherically and elliptically shaped voids embedded in a SiC substrate. Here, α_{0i} stands for the polarizability in the MLWA regime of the *i*th semi axis of the ellipsoid, while k is the normal incidence wavenumber. The correspondent polarizability is given as $\alpha_{0i} = \alpha_i\left(1 - \frac{k^2\alpha_i}{4\pi a_i} - \frac{ik^3\alpha_i}{6\pi}\right)^{-1}$, where a_i ($i = 1, 2, 3$) are the semi axes of the ellipsoid. The calculated resonant frequencies $\omega_1^{MLWA}/2\pi c = 900$ cm^{-1} for an oblate spheroid ($a_1 = a_2$) [Fig. S2(a)] and

$\omega_1^{MLWA}/2\pi c = 859\ \mathrm{cm}^{-1}$ and $\omega_2^{MLWA}/2\pi c = 883\ \mathrm{cm}^{-1}$ for an ellipsoidal particle [Fig. S2(b)] are in good agreement with the experiment. The resonances exhibit a strong linear polarization along the direction of the small axes of the antenna [a_3 in Fig. S2(a) and a_1, a_3 in Fig. S2(b)], whereas for the long axes [a_1, a_2 in Fig. S2(a) and a_2 in Fig. S2(b)], the polarization is negligible. Such a polarization anisotropy is essential for the geometric phase accumulation in the anisotropic QCM.

3 (a). Transmission spectra of SPP-based QCMs

The transmission spectra of the QCMs based on nanoantennas in thin metal film were additionally studied in the visible spectrum via the excitation of SPPs. The QCMs with $d = 550\ \mathrm{nm}$, sandwiched between a glass substrate and a glass slide on the top, were normally illuminated by a supercontinuum light source (Fianium SC-450-4) and the zero-order transmitted light was collected by a spectrometer. The SPPs are resonantly excited when the momentum conservation is fulfilled; thus, the correspondent $\mathbf{k}_{SPP}$ matches the relevant circle of QC reciprocal vectors at different wavelengths. The measured transmission spectrum of the isotropic QCM [Fig. S3 top spectrum] exhibits a single resonance dip at 700 nm corresponding to the reciprocal vector set $\mathbf{G}_1$. The anisotropic QC configuration reveals an additional resonant dip at a longer wavelength of 810 nm corresponding to the reciprocal vector set $\mathbf{G}_2$ [Fig. S3 bottom spectrum]. Note that this result purely arises from the geometric phase (See section 3(b)). The obtained dip wavelengths are in good agreement with the theoretical values $\lambda_{1,2} = 2\pi\sqrt{\varepsilon_1\varepsilon_2/(\varepsilon_1+\varepsilon_2)}/\left|\mathbf{G}_{1,2}\right| = 690$ and 810 nm, where $\varepsilon_{1,2}$ stand for the glass and gold permittivity, respectively. Moreover, the inset of Fig. S3 shows the calculated finite difference time domain (FDTD) transmission spectra confirming

the experimental results. The three additional modes with smaller wavevectors $\mathbf{G}_{3,4,5}$ cannot be detected within the restricted experimental spectral window and for this reason do not appear in Fig. S3.

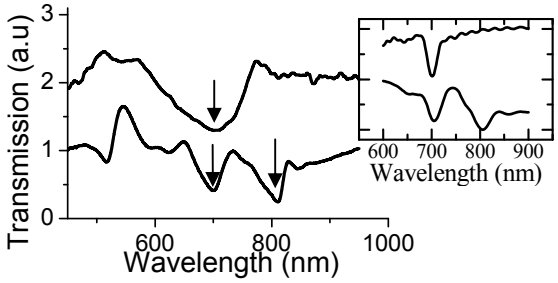

FIG. S3. Measured and calculated (inset) transmission spectra through the isotropic (top curve) and the anisotropic (bottom curve) SPP-based QCMs with extent of 40-by-40-μm^2. Apertures with the same dimensions as in Figs. 2(a) and 2(b) were perforated in a 250 nm thick Au film.

3(b). Comparison between modes of homogenous anisotropic and inhomogeneous anisotropic QCMs

We performed finite difference time domain (FDTD) simulations to compare the modes of the homogenous and inhomogenous orientation of nanoantennas in the anisotropic QCMs. The modes were evaluated by examining the antiresonance dips in the reflection spectrum. These dips result from the absorption to surface plasmon polaritons waves. Two quasicrystal structures having the same nanoantennas positions and different sets of orientations were simulated. The nanoantennas in the first structure were oriented along the tiling grid [see Fig. S4(b)], while the nanoantennas in the second structure have uniform orientation [see Fig. S4(a)]. Normal illumination with circularly polarized light on the inhomogeneous QCM reveals a resonance dip at

~700 nm, corresponding to the reciprocal vectors of the QCM, and two additional resonant dips at longer wavelengths of 810 nm and 950 nm, that correspond to the aperiodic orientations of the antennas [see black curve in Fig. S4(c)]. We conducted reflection simulations to find the spectrum of homogenous QCM, which is illuminated by circularly polarized light. Such an illumination reveals a broadband absorption (~150 nm), which is a signature of the local resonance of the nanoantennas and is not related to the collective modes [Fig. S4(c) blue curve].

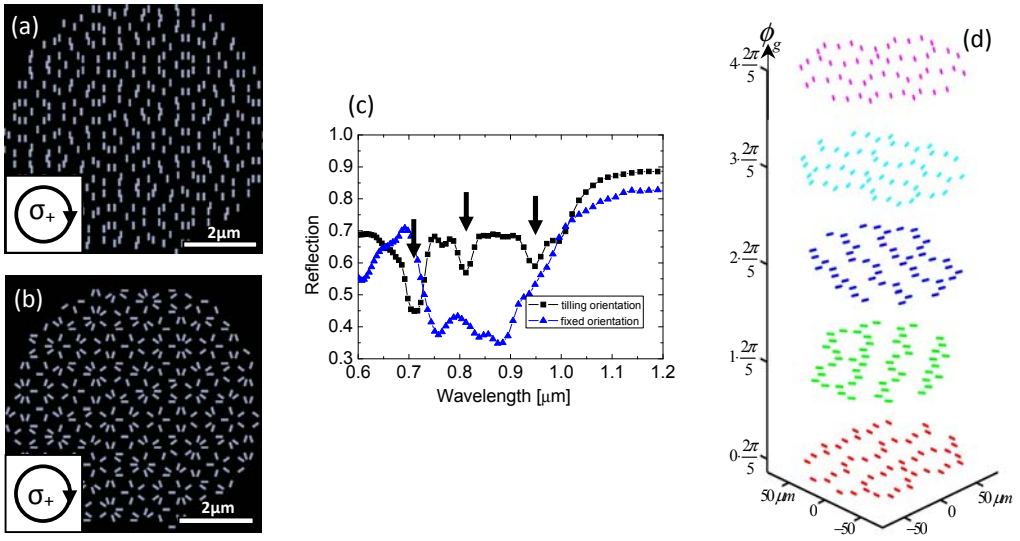

FIG. S4. Simulated reflection spectra of homogenous anisotropic QCM and inhomogeneous anisotropic QCM. (a,b) The simulated quasicrystal structures with nanoantennas oriented along the tiling grid (b) and in fixed orientation (a). The inset depicts the illuminated light polarization of each configuration. (c) The simulated reflection. The black arrows correspond to the absorption modes of the inhomogeneous QCM, while the blue curve denotes the reflection spectrum of the homogeneous QCM. (d) Five-level quantized geometric phase of the inhomogeneous

anisotropic QCM. Each color level corresponds to the same phase pickup (attached value at the left) from the equally oriented antennas.

4. Far-field radiation from the anisotropic QCM

In order to characterize the scattering field from the anisotropic QCM, we consider a single anisotropic antenna as a radiating dipole $\mathbf{p}_\theta = \left(p_{\theta x}, p_{\theta y}\right)$ located at $\mathbf{r}$ in the x-y interface between dielectric ($z > 0$) and polar ($z < 0$) media and oriented with an angle θ with respect to x axis (see Fig. S5).

It has been shown that the scattering field in the radiation zone can be written as [see Ref. S2]

$$\mathbf{E} \propto \frac{e^{i\mathbf{k}\cdot(\mathbf{R}-\mathbf{r})}}{|\mathbf{R}-\mathbf{r}|}\left[(\hat{\mathbf{m}}\times\mathbf{p}_\theta)\times\hat{\mathbf{m}}\right], \tag{S1}$$

where $|\mathbf{k}| = \frac{2\pi}{\lambda}$, $\hat{\mathbf{m}}$ is the unit vector in the direction of the point of observation D and $\mathbf{R}$ is the vector directing to this point from the origin O. By assuming that $kR >> 1$, we obtain that $\hat{\mathbf{m}} \approx \hat{\mathbf{z}}$, thus Eq. S1 takes the form

$$\mathbf{E} \propto \frac{e^{i\mathbf{k}\cdot\mathbf{R}}}{|\mathbf{R}|} e^{-i\mathbf{k}\cdot\mathbf{r}} \mathbf{p}_\theta . \tag{S2}$$

We express the dipole moment of an anisotropic antenna exited by an incident light $\mathbf{E}_{in}$ via the polarizability tensor $\vec{\alpha}_\theta$ as

$$\mathbf{p}_\theta = \vec{\alpha}_\theta \mathbf{E}_{in} . \tag{S3}$$

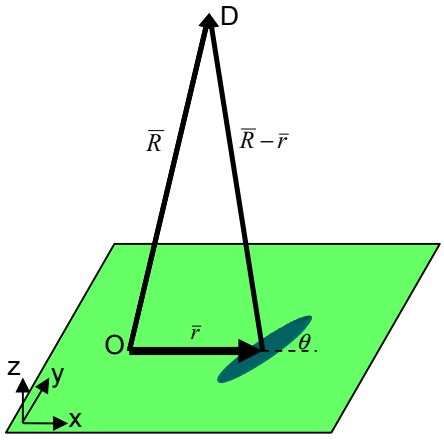

FIG. S5. Schematic setup of the radiating dipole.

The polarizability tensor of the nanoantenna, oriented with its long axis parallel to the x direction, can be written as

$$\vec{\alpha}_0 = \alpha \begin{pmatrix} 1 & 0 \\ 0 & 0 \end{pmatrix}, \tag{S4}$$

while the polarizability tensor of the nanoantenna oriented at an angle θ is given by

$$\vec{\alpha}_\theta = \alpha \begin{pmatrix} \cos\theta & -\sin\theta \\ \sin\theta & \cos\theta \end{pmatrix} \begin{pmatrix} 1 & 0 \\ 0 & 0 \end{pmatrix} \begin{pmatrix} \cos\theta & \sin\theta \\ -\sin\theta & \cos\theta \end{pmatrix}. \tag{S5}$$

This transformation yields that

$$\vec{\alpha}_\theta = \frac{\alpha}{2} \begin{pmatrix} 1 & 0 \\ 0 & 1 \end{pmatrix} + \frac{\alpha}{2} \begin{pmatrix} \cos 2\theta & \sin 2\theta \\ \sin 2\theta & -\cos 2\theta \end{pmatrix}. \tag{S6}$$

For convenience, we adopt the Dirac bra-ket notation and convert $\vec{\alpha}_\theta$ to the helicity basis in which $|\sigma_+\rangle = \begin{pmatrix} 1 \\ 0 \end{pmatrix}$ and $|\sigma_-\rangle = \begin{pmatrix} 0 \\ 1 \end{pmatrix}$ are the two-dimensional unit vectors for right-handed and left-handed circular polarizations, respectively. In this

basis, the polarizability is described by the matrix $\ddot{\alpha}_\theta^h = \mathbf{U}\ddot{\alpha}_\theta\mathbf{U}^{-1}$, where $\mathbf{U} = \frac{1}{\sqrt{2}}\begin{pmatrix} 1 & i \\ 1 & -i \end{pmatrix}$ is a unitary conversion matrix. The explicit calculation yields that

$$\ddot{\alpha}_\theta^h = \frac{\alpha}{2}\begin{pmatrix} 1 & 0 \\ 0 & 1 \end{pmatrix} + \frac{\alpha}{2}\begin{pmatrix} 0 & e^{i2\theta} \\ e^{-i2\theta} & 0 \end{pmatrix}. \tag{S7}$$

Thus, for an incident plane wave with an arbitrary polarization $|E_{in}\rangle$, we find that the resulting field is

$$|E_{out}\rangle \propto \frac{e^{i\mathbf{k}\cdot\mathbf{R}}}{|\mathbf{R}|} e^{-i\mathbf{k}\cdot\mathbf{r}} \left(|E_{in}\rangle + e^{i2\theta}\langle E_{in}|\sigma_-\rangle|\sigma_+\rangle + e^{-i2\theta}\langle E_{in}|\sigma_+\rangle|\sigma_-\rangle \right). \tag{S8}$$

The contribution from all nanoantennas located at $\mathbf{r}_n$ and with corresponding orientation angles $\theta(\mathbf{r}_n)$ in the anisotropic QCM results in the total field distribution which is given by

$$|E_{out}^{total}(\mathbf{k})\rangle \propto \frac{e^{i\mathbf{k}\cdot\mathbf{R}}}{|\mathbf{R}|} \sum_n e^{-i\mathbf{k}\cdot\mathbf{r}_n} \left(|E_{in}\rangle + e^{i2\theta(\mathbf{r}_n)}\langle E_{in}|\sigma_-\rangle|\sigma_+\rangle + e^{-i2\theta(\mathbf{r}_n)}\langle E_{in}|\sigma_+\rangle|\sigma_-\rangle \right), \tag{S9}$$

or alternatively,

$$|E_{out}^{total}(\mathbf{k})\rangle \propto f_0|E_{in}\rangle + f_+\langle E_{in}|\sigma_-\rangle|\sigma_+\rangle + f_-\langle E_{in}|\sigma_+\rangle|\sigma_-\rangle. \tag{S10}$$

Here, $f_0 = \hat{F}\left\{\sum_n \delta(\mathbf{r}-\mathbf{r}_n)\right\}$ and $f_\pm = \hat{F}\left\{\sum_n \delta(\mathbf{r}-\mathbf{r}_n)e^{\pm i2\theta(\mathbf{r}_n)}\right\}$. Equation S10 shows that $|E_{out}^{total}(\mathbf{k})\rangle$ comprises three polarization orders: the $|E_{in}\rangle$, $|\sigma_+\rangle$ and $|\sigma_-\rangle$. The $|E_{in}\rangle$ polarization order maintains the polarization and phase of the incident beam, whereas the phases of $|\sigma_\pm\rangle$ polarization orders is equal to $\pm 2\theta$, respectively. Note that the phase modification of the $|\sigma_+\rangle$ and $|\sigma_-\rangle$ polarization orders results solely from local changes in polarization and is therefore, geometric in nature.

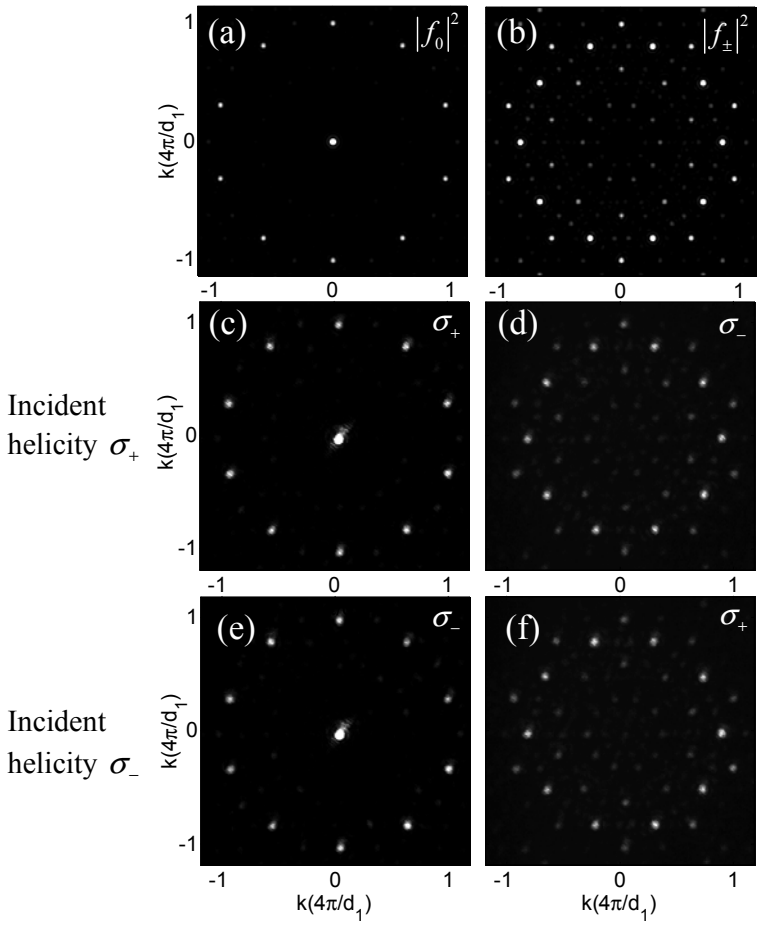

FIG. S6. (a,b) Calculated $|f_0|^2$ (a) and $|f_\pm|^2$ (b) corresponding to the first term (incident helicity component) and the second term (spin-flip component) of Eqs. S11 and S12. (c-f) Measured diffraction patterns of the two helicity components of the anisotropic QCM for incident spin state $|\sigma_+\rangle$ (c,d) and incident spin state $|\sigma_-\rangle$ (e,f). Measured diffraction patterns of the incident helicity component (c,e) and the spin-flip component (d,f). $\sigma_\pm$ in the figures denote the spin-projected states of the measured diffracted waves. Note that the examined QCM was the same as presented in Fig. 2(b) with the same experimental parameters.

For the incident spin state of $|\sigma_+\rangle$, Eq. S10 can be expressed as

$$\left|E_{total}^{\sigma_+}(\mathbf{k})\right\rangle \propto f_0|\sigma_+\rangle + f_-|\sigma_-\rangle, \tag{S11}$$

while for the incident spin state of $|\sigma_-\rangle$, Eq. S10 is given by

$$\left|E_{total}^{\sigma_-}(\mathbf{k})\right\rangle \propto f_0|\sigma_-\rangle + f_+|\sigma_+\rangle. \tag{S12}$$

The presented model exhibits a good agreement with the observation of the field scattered from the anisotropic QCMs. The first term of Eqs. S11 and S12 ushers in the diffraction pattern [Fig. S6(a)] of the field with the incident helicity component, and it confirms the measured single circle of modes [Fig. 2(f) and Figs. S6(c) and S6(e)]. The emerging spin-flip component leads to the calculated diffraction pattern [Fig. S6(b)] which is the signature of the geometric phase modes manifested by the five circles, confirming the measured diffractions for the incident spin states of $|\sigma_+\rangle$ [Fig. 2(h) and Fig. S6(d)] and $|\sigma_-\rangle$ [Fig. S6(f)].

5. Optical spin-Hall effect for different outcomes of the randomization process

For a random selection of half of the anisotropic nanoantennas in the QCMs, we obtained a part of the QCM for which the orientations would be distorted. By the repeated random process of the antenna orientations configuration, we achieved an outcome, where spin-dependent modes are obtained on the circle of radius $|\mathbf{G}_3|$ [Figs. S7(a), S7(b) and S7(e)]. This spin-dependent diffraction pattern demonstrates the optical spin-Hall effect (OSHE) in the perturbed anisotropic QCM. The QCM was illuminated with right and left circularly polarized light at the wavelength of $\lambda = 750\,\text{nm}$ and the OSHE was observed experimentally [Figs. S7(c)-S7(e)]. The

efficiency of the OSHE becomes significant when half of the antenna defects are introduced in the structure [Fig. S7 (f)].

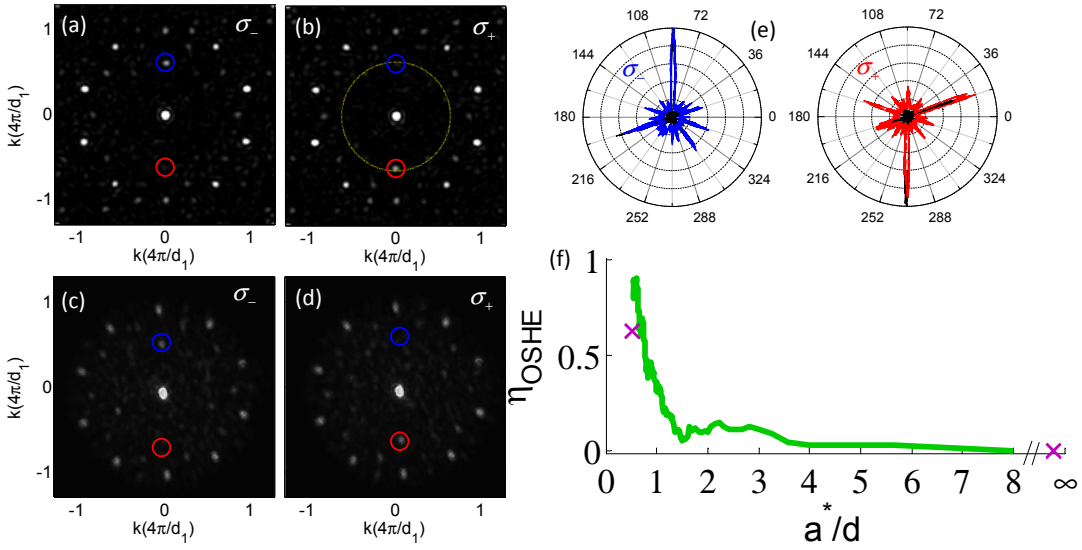

FIG. S7. (a-d) Calculated (a,b) and measured (c,d) diffraction patterns of the QCM with the geometric phase defects. The patterns reveal the spin-dependent modes, located on the $|\mathbf{G}_3|$ circle, for σ_- (a,c) and σ_+ (b,d) illuminations, respectively. Blue and red guiding rings highlight the location of the spin-dependent modes in the reciprocal space for each helicity $\sigma_\pm$. (e) Azimuthal cross sections of measured (red and blue) and calculated (black) intensities for $\sigma_\pm$ illuminations. The intensities were measured along the yellow circle in (b). In this polar representation, the azimuthal angle is given in degrees and the intensity is on a linear scale. (f) Dependence of the OSHE efficiency η_{OSHE} on the normalized average distance between defects a^*/d. The green curve corresponds to the calculated efficiency for the specific randomization process and the experimental points are denoted by purple crosses.

[S1] K. D. Ko and C. K. Toussaint, J. Quant. Spectrosc. Radiat. Transf. **110** (12), 1037 (2009).

[S2] J. D. Jackson, *Classical Electrodynamics,* Third Edition (John Wiley & Sons, Inc., 1999).